Predictive Direct Control of Nine-Switch Converter Unified Power Quality Conditioner Based on Time-Sharing Cooperative Control

Guifeng Wang, *Member, IEEE*, Yunhui Jiang, Zhan Liu, *Member, IEEE*, Yiming Ma, and Jianfei Wang

***Abstract*—In order to solve problems present in traditional indirect control in the nine-switch converter unified power quality conditioner (NSC-UPQC), such as response delay caused by harmonic detection and phase-locked loop (PLL), system coupling caused by coordinate transformations as well as difficulties in tuning proportional-integral (PI) controller parameters. A predictive direct control strategy based on time-sharing cooperative control (TSCC) was hereby proposed for NSC-UPQC. The strategy integrated the NSC topology working principle, and the cooperative control concept was introduced. In the first place, a mathematical model was established for the UPQC predictive direct control system in the $\alpha\beta$ coordinate system. This model was formulated based on an analysis of the configuration and operational principles of the NSC-UPQC system, incorporating principles of direct control and finite set model predictive control. Besides, the power balance principle and dead-beat control principle were employed to construct the mechanisms for generating reference currents on the series and parallel sides. This method avoided the complexities associated with coordinate transformations and PLL detection, eliminating the need for harmonic detection and PI controller parameter tuning. As a result, it effectively simplified the control system structure and enhanced the dynamic response capability of the system. On such a basis, the concept of cooperative control was introduced, leveraging the redundancy of the NSC-UPQC topology switches. Additionally, the principles for vector selection and control mechanisms under TSCC were presented, and coordinated control on the series and parallel sides of NSC-UPQC was achieved, considerably enhancing the precision of system control. Finally, detailed simulation and hardware-in-loop test analyses of the proposed strategy were conducted, further validating its feasibility and effectiveness.**

***Index Terms*—Nine-switch converter (NSC), predictive direct control, reference current, time-sharing cooperative control (TSCC), unified power quality conditioner (UPQC).**

I. Introduction

With the widespread application of power electronic devices and nonlinear loads, power distribution systems have been exposed to power quality issues, such as voltage fluctuations, surges, harmonic distortion and imbalance [1], [2], [3]. Commonly used voltage and current compensation devices include static synchronous compensators, series active power filters (SAPF), parallel active power filters (PAPFs) and dynamic voltage restorers [4], [5], [6], [7]. However, these devices often have limited functions in power quality management and fail to meet the diverse demands of coordinated control for various power quality problems. The unified power quality conditioner (UPQC) merges SAPF and PAPF characteristics, allowing it to effectively address a spectrum of power quality issues. This unique capability has earned UPQC widespread recognition from researchers globally [8].

However, the traditional UPQC adopts a back-to-back converter topology, which is complex and relatively expensive, severely limiting its application in various fields. By replacing the back-to-back converter circuit topology in UPQC with the nine-switch converter (NSC), the number of switching devices can be reduced by 25%, boasting advantages such as lower cost, smaller size, reduced losses, etc. [9]. Currently, scholars worldwide primarily focus on several aspects of NSC-UPQC research, including the development of rational, reliable, and effective modulation and control methods. Additionally, efforts are directed towards enhancing the utilization efficiency of the dc voltage.

Specifically, Mabusubani and Shaik employed a classic dual-loop control strategy based on a proportional-integral (PI) controller, achieving compensation for current and voltage through time-sharing control (TSC) in [10]. Based on this article, a hybrid modulation strategy was proposed in [11]. This strategy divided the dc bias in the modulation signal into two parts: the fundamental frequency bias selected according to the same frequency mode and the harmonic bias determined in advance based on the harmonic capacity to be compensated by the system. This method combined the advantages of same-frequency and different-frequency modes, reducing the required dc voltage on the converter side. As for improving the utilization of dc voltage, an approach of serially connecting a monotonic harmonic filtering branch to the equivalent parallel side of the NSC-UPQC was proposed. By reducing the fundamental frequency component of the ac grid borne by the equivalent parallel side, this method lowered the amplitude of the dc voltage on the NSC-UPQC side. In [12], the researchers applied

Received 5 January 2024; revised 2 April 2024 and 27 June 2024; accepted 17 July 2024. Date of publication 29 July 2024; date of current version 28 January 2025. This work was supported in part by the National Natural Science Foundation of China under Grant 51707086 and in part by Postgraduate Research and Practice Innovation Program of Jiangsu Province under Grant kycx23_2913. *(Corresponding author: Yiming Ma.)*

The authors are with the School of Electrical Engineering and Automation, Jiangsu Normal University, Xuzhou 221116, China (e-mail: 6020160105@jsnu.edu.cn; 2020221749@jsnu.edu.cn; liuzhan@jsnu.edu.cn; 2020211627@jsnu.edu.cn; 2020221813@jsnu.edu.cn).

Color versions of one or more figures in this article are available at https://doi.org/10.1109/TPEL.2024.3435052.

Digital Object Identifier 10.1109/TPEL.2024.3435052

NSC-UPQC to a doubly-fed wind power system, achieving flexible fault ride-through under various voltage conditions. In order to leverage the distinct characteristics of voltage compensation and current compensation while meeting dc voltage requirements, they developed a dynamic modulation ratio optimization strategy aimed at enhancing dc voltage utilization. Apart from sinusoidal pulsewidth modulation (SPWM) methods, some scholars proposed the application of space vector pulse width modulation (SVPWM) for NSC-UPQC based on the relationship between NSC and the voltage vectors of traditional two-level inverters [9]. They analyzed the NSC action vectors and the corresponding action times, proposing a control method according to the instantaneous power theory.

Intelligent control algorithms were also incorporated into NSC-UPQC. For instance, fuzzy control was utilized to determine the value of *Kp*, with simulation results confirming its effectiveness [13]. Additionally, in [14], particle swarm optimization techniques were employed to enhance the operational speed of the NSC-UPQC system, resulting in a 33% reduction in switch stress.

In summary, the above studies have primarily employed indirect control as the macro implementation strategy for UPQC by adopting the SPWM and SVPWM techniques [15]. Indirect control focuses on voltage and current compensation as control objectives, making its goals more direct and concepts clearer. However, it involves harmonic detection, leading to phase lag and filtering delays. By contrast, direct control strategies eliminate the need for harmonic detection [16], controlling the series converter as a sine current source and the parallel converter as a sine voltage source separately. In this case, the controller structure is effectively simplified, which further promotes the dynamic performance of the system. Currently, NSC-UPQC control strategies frequently rely on linear control algorithms based on synchronous rotating coordinate systems, leading to substantial internal coupling. These strategies are susceptible to the accuracy of the phase-locked loop (PLL), and parameter tuning can present challenges.

Finite control set model predictive control (FCS-MPC)$*$ combines nonlinearity and system constraints, eliminating the need for traditional PWM modulation [17], [18], [19]. This approach provides substantial intuitiveness and flexibility, offering a fresh perspective for optimizing the control strategy of NSC-UPQC. In [20], FCS-MPC was implemented in NSC-UPQC, with a focus on harmonic compensation under nonlinear and unbalanced load conditions. However, it did not address issues, such as voltage sag, swell, and power coordination distribution. In the application of FCS-MPC to NSC, a common approach generally involves combining the value functions of the upper and lower output terminals into a single value function [21]. Nevertheless, this approach not only increases the computational burden on the system, but also fails to achieve independent control of the two output terminals. On the other hand, while the TSC method achieves independent control of both ends, it only operates one output terminal at any given moment, resulting in decreased tracking accuracy for the specified current [22].

To address the issues in traditional indirect control, such as response delay caused by harmonic detection and PLL, system coupling due to coordinate transformations, and difficulties in PI parameter tuning, and to improve the tracking accuracy of NSC for reference currents at the same time, a predictive direct control strategy was hereby proposed on the basis of a time-sharing cooperative control (TSCC) approach suitable for NSC-UPQC. The main contributions of this research are as follows.

1) The mathematical model of the NSC-UPQC predictive direct control system in the $\alpha\beta$ coordinate system was established, along with the mechanism for generating reference currents. This created a system free from harmonic detection, PLL, or closed-loop control. It removed the necessity for six PI controllers found in traditional linear control methods, thereby mitigating potential empirical and subjective aspects that may arise when configuring PI parameters.
2) By leveraging the topological characteristics of NSC switch devices and introducing a cooperative control concept based on TSC, principles and control mechanisms for TSCC were also established. This enabled coordinated control of the two output terminals and achieved superior tracking accuracy for the specified currents.

The rest of this article is organized as follows. Section II presents the topology and working principles of NSC-UPQC. Section III covers the design of the NSC-UPQC direct control predictive model, the mechanism for generating reference currents as well as the design of value functions based on the $\alpha\beta$ coordinate system. Section IV elucidates the TSCC vector selection principles, establishing a cooperative control mechanism. Section V validates the feasibility of the proposed control strategy through simulation and hardware-in-loop test analysis. Finally, Section VI concludes this article.

II. Topology and Working Principle of NSC-UPQC

A. Topology of NSC-UPQC

The NSC-UPQC topology is illustrated in Fig. 1. The figure shows the supply voltage u_{sabc}, the supply current i_{sabc}, the load voltage u_{Labc}, the load current i_{Labc}, the series transformer compensation voltage u_{cabc}, the series transformer secondary side current i_{cabc1}, the parallel side compensation current i_{cabc2}. u_{1abc}, u_{2abc} represent series and parallel side output voltages, whereas i_{abc1}, i_{abc2} represent series and parallel side output current, respectively. Additionally, C_1, C_2 and L_1, L_2 indicate filter capacitors and filter inductors for series and parallel side respectively. The dc side capacitance is denoted by $C_{\rm dc}$, while the dc-bus voltage is denoted by $V_{\rm dc}$.

The NSC topology is shown within the dashed line in Fig. 1, with a total of three bridge arms, and three switching devices on each bridge arm for a total of nine switching devices. The key feature of NSC lies in utilizing switching device multiplexing to combine the lower tubes of one converter with the upper tubes of the other converter in the conventional back-to-back 12-switching converter, thereby reducing the total number of switching devices. S_{AU}, S_{BU}, S_{CU} and S_{AM}, S_{BM}, S_{CM} constitute the upper side converter INV1 as the UPQC parallel side converter, while S_{AM}, S_{BM}, S_{CM} and S_{AL}, S_{BL}, S_{CL} constitute the lower side converter INV2 as the UPQC series side converter.

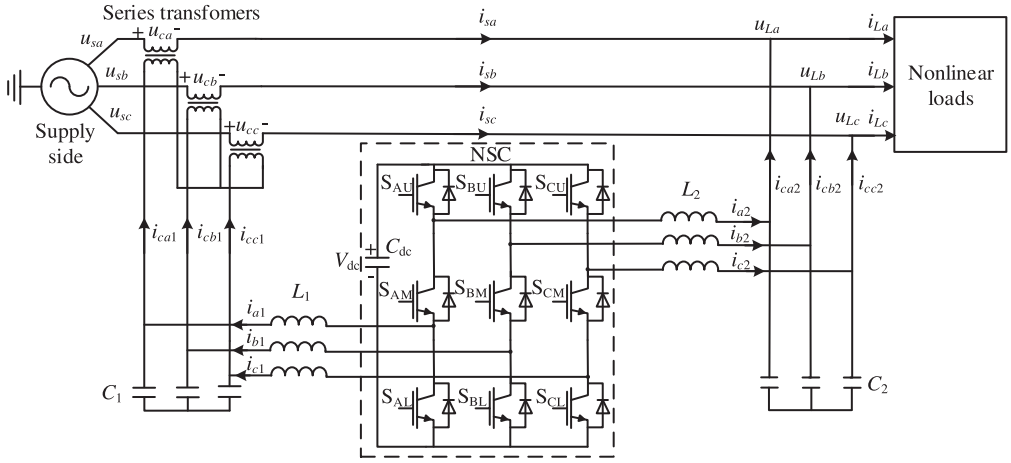

Fig. 1. Topology structure of NSC-UPQC.

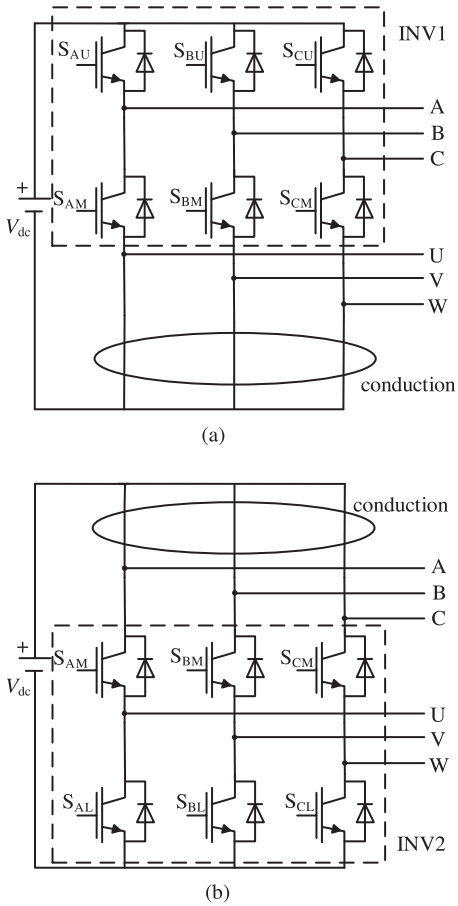

Fig. 2. TSC principle of NSC. (a) INV1 work. (b) INV2 work.

B. Working Principles of NSC

TSC principle of NSC is presented in Fig. 2. When INV1 operates, the lower tube of each phase of the bridge arm always maintains conduction, when, INV1 can be equated to a two-level inverter. When INV2 works, the upper tube of each phase of the bridge arm always maintains conduction, when, INV2 can be equated to a two-level inverter. Independent control of the two outputs is thus realized.

TABLE I
ALL VALID STATES OF NSC

State	S_{XU}	S_{XM}	S_{XL}	u_{X2}	u_{X1}
1	1	0	1	V_{dc}	0
2	0	1	1	0	0
3	1	1	0	V_{dc}	V_{dc}

In order to prevent the short circuit on the dc side and to form an effective working circuit with the load, there are two constraints in the NSC [23].

1) There should be two switching devices on at the same moment in the same bridge arm.
2) The output voltage at the upper end should be higher than or equal to that at the lower end at any moment.

Table I gives all the possible switching states and port output voltages for each phase, where the switching device conduction state is noted as 1, the off state is 0, X is taken as a, b, c, and u_{X2}, u_{X1} are the INV1, INV2 output voltages respectively. As given in Table I, three active states per phase are involved in the NSC, totaling 27 switching state combinations.

As given in Table I, the relationship between output voltages on the series side, the switching device state and dc-bus voltage can be expressed as follows:

$$\begin{cases} u_{a1} = (1-S_{AL})\,V_{dc} \\ u_{b1} = (1-S_{BL})\,V_{dc}. \\ u_{c1} = (1-S_{CL})\,V_{dc} \end{cases} \tag{1}$$

The relationship between output voltages on the parallel side, the switching device state and dc-bus voltage can be expressed as follows:

$$\begin{cases} u_{a2} = S_{AU}V_{dc} \\ u_{b2} = S_{BU}V_{dc}. \\ u_{c2} = S_{CU}V_{dc} \end{cases} \tag{2}$$

III. Predictive Direct Control of NSC-UPQC

According to the UPQC direct control principle, the series side converter is controlled as a sinusoidal current source, while the parallel side converter is controlled as a sinusoidal voltage source without the harmonic detection link. Thus, predictive direct control can be directly modeled in the $\alpha\beta$ coordinate system, avoiding the synchronous rotating coordinate transformation and its induced problems of system coupling and affected by the precision of PLL. Reference currents generation mechanism is deduced and established based on the principle of system power balancing and dead-beat control, thereby basically achieving the PI-free outer loop control while avoiding the complex PI parameter adjustment.

A. Modeling on Predictive Control of NSC-UPQC

The control strategy proposed in this article requires the inductance on the series and parallel sides, as well as the capacitance on the parallel side, as part of the mathematical model. However, the capacitance C_1 on the series side is not actually necessary as a component of the mathematical model used in the control strategy and plays a minor role in the entire control system. Therefore, it can be considered negligible or simply ignored. The mathematical model of the series converter in the $\alpha\beta$ coordinate system can be obtained based on KVL and KCL

$$\begin{cases} \frac{di_{\alpha1}}{dt} = \frac{1}{L_1}u_{\alpha1} - \frac{1}{L_1}u_{c\alpha} \\ \frac{di_{\beta1}}{dt} = \frac{1}{L_1}u_{\beta1} - \frac{1}{L_1}u_{c\beta} \end{cases} \tag{3}$$

where the α-axis component and β-axis component of series side output voltage $u_{\alpha1}$, $u_{\beta1}$, the α-axis component and β-axis component of series side output current $i_{\alpha1}$, $i_{\beta1}$, the α-axis component and β-axis component of the grid compensation voltage $u_{c\alpha}$, $u_{c\beta}$.

Since the value of filter capacitor C_2 on the parallel side is large and cannot be neglected, the mathematical model of UPQC parallel converter in the $\alpha\beta$ coordinate system can be obtained as

$$\begin{cases} \frac{du_{L\alpha}}{dt} = \frac{1}{C_2}i_{\alpha2} - \frac{1}{C_2}i_{c\alpha2} \\ \frac{du_{L\beta}}{dt} = \frac{1}{C_2}i_{\beta2} - \frac{1}{C_2}i_{c\beta2} \end{cases} \tag{4}$$

$$\begin{cases} \frac{di_{\alpha2}}{dt} = \frac{1}{L_2}u_{\alpha2} - \frac{1}{L_2}u_{L\alpha} \\ \frac{di_{\beta2}}{dt} = \frac{1}{L_2}u_{\beta2} - \frac{1}{L_2}u_{L\beta} \end{cases} \tag{5}$$

where the α-axis component and β-axis component of parallel side output voltage $u_{\alpha2}$, $u_{\beta2}$, the α-axis component and β-axis component of parallel side output current $i_{\alpha2}$, $i_{\beta2}$, the α-axis component and β-axis component of the load voltage $u_{L\alpha}$, $u_{L\beta}$, the α-axis component and β-axis component of parallel side compensation current $i_{c\alpha2}$, $i_{c\beta2}$.

After discretizing (3) and (5), the series and parallel side prediction models are obtained as follows:

$$\begin{cases} i_{\alpha1}(k+1) = i_{\alpha1}(k) - \frac{T_s}{L_1}u_{c\alpha}(k) + \frac{T_s}{L_1}u_{\alpha1}(k) \\ i_{\beta1}(k+1) = i_{\beta1}(k) - \frac{T_s}{L_1}u_{c\beta}(k) + \frac{T_s}{L_1}u_{\beta1}(k) \end{cases} \tag{6}$$

$$\begin{cases} i_{\alpha2}(k+1) = i_{\alpha2}(k) - \frac{T_s}{L_2}u_{L\alpha}(k) + \frac{T_s}{L_2}u_{\alpha2}(k) \\ i_{\beta2}(k+1) = i_{\beta2}(k) - \frac{T_s}{L_2}u_{L\beta}(k) + \frac{T_s}{L_2}u_{\beta2}(k) \end{cases} \tag{7}$$

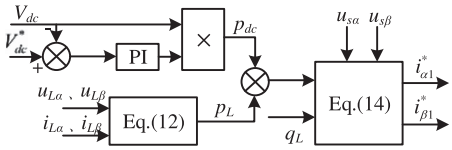

Fig. 3. Reference current generation mechanism of series side.

where T_s is the discretization period, $y(k)$ denotes the value of variable y in the kT_s period, and $y(k)$ refers to the value of variable y in the $(k+1)T_s$ period.

B. Reference Current Generation Mechanism

The power balance of the UPQC system should be regulated by a current command on the series side. Assuming p_{in} as the total power from the grid side, the system power balance can be achieved as

$$p_{\text{in}} = u_s g i_s = (u_L + u_c) g i_s. \tag{8}$$

Since $i_s = i_L$-i_{c2}, (8) can be replaced as

$$p_{\text{in}} = u_L g i_L - u_L g i_{c2} + u_c g i_s. \tag{9}$$

Taking $p_{\text{dc}} = -u_L g i_{c2} + u_c g i_s$ as a system loss, it can be compensated by the dc side control

$$p_{\text{in}} = u_L g i_L + p_{\text{dc}}. \tag{10}$$

Transforming (10) to the $\alpha\beta$ coordinate system

$$\begin{bmatrix} u_{s\alpha} & u_{s\beta} \\ u_{s\beta} & -u_{s\alpha} \end{bmatrix} \begin{bmatrix} i_{s\alpha} \\ i_{s\beta} \end{bmatrix} = \begin{bmatrix} u_{L\alpha} & u_{L\beta} \\ u_{L\beta} & -u_{L\alpha} \end{bmatrix} \begin{bmatrix} i_{L\alpha} \\ i_{L\beta} \end{bmatrix} + \begin{bmatrix} p_{\text{dc}} \\ 0 \end{bmatrix}. \tag{11}$$

Based on the generalized instantaneous reactive power theory [24], the relationship between the instantaneous active power p_L, instantaneous reactive power q_L and the load voltage and current in the $\alpha\beta$ coordinate system can be obtained as

$$\begin{bmatrix} p_L \\ q_L \end{bmatrix} = \begin{bmatrix} u_{L\alpha} & u_{L\beta} \\ u_{L\beta} & -u_{L\alpha} \end{bmatrix} \begin{bmatrix} i_{L\alpha} \\ i_{L\beta} \end{bmatrix}. \tag{12}$$

Substituting (12) into (11) yields

$$\begin{bmatrix} u_{s\alpha} & u_{s\beta} \\ u_{s\beta} & -u_{s\alpha} \end{bmatrix} \begin{bmatrix} i_{s\alpha} \\ i_{s\beta} \end{bmatrix} = \begin{bmatrix} p_L + p_{\text{dc}} \\ q_L \end{bmatrix}. \tag{13}$$

To ensure no reactive power input to the series side, the reference reactive power q_L is set as 0. Thus, the reference current of series side can be obtained as

$$\begin{cases} i_{\alpha1}^* = i_{s\alpha}^* = \frac{u_{s\alpha}(p_L + p_{\text{dc}})}{u_{s\alpha}^2 + u_{s\beta}^2} \\ i_{\beta1}^* = i_{s\beta}^* = \frac{u_{s\beta}(p_L + p_{\text{dc}})}{u_{s\alpha}^2 + u_{s\beta}^2} \end{cases}. \tag{14}$$

The output current generation mechanism of the series side is shown in Fig. 3.

Discretizing and organizing (4) yields a reference value for the reference current on the parallel side

$$\begin{cases} i_{\alpha2}^*(k) = i_{c\alpha2}(k) + \frac{C_2}{T_s}\left(u_{L\alpha}(k+1) - u_{L\alpha}(k)\right) \\ i_{\beta2}^*(k) = i_{c\beta2}(k) + \frac{C_2}{T_s}\left(u_{L\beta}(k+1) - u_{L\beta}(k)\right) \end{cases}. \tag{15}$$

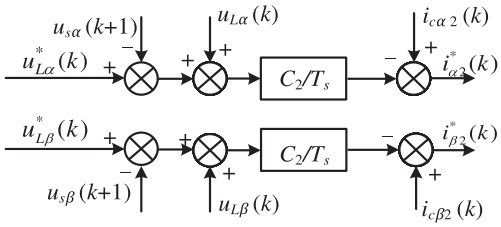

Fig. 4. Reference current generation mechanism of parallel side.

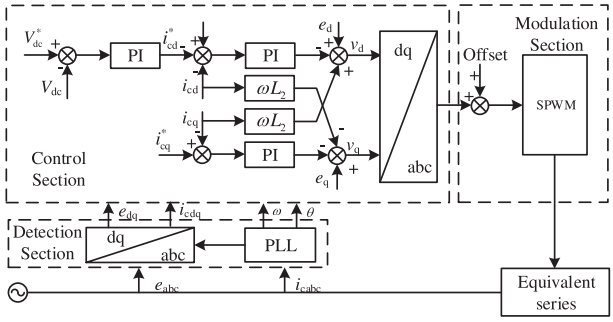

Fig. 5. Block diagram of traditional control.

According to the principle of deadbeat control, assuming that the load voltage perfectly tracks the desired ideal voltage in the k+1st sampling period, then

$$u_L(k+1) = u_L^*(k). \tag{16}$$

Equation (15) can be transformed as

$$\begin{cases} i^*_{\alpha 2}(k) = i_{c\alpha 2}(k) + \frac{C_2}{T_s}\left(u^*_{L\alpha}(k) - u_{L\alpha}(k)\right) \\ i^*_{\beta 2}(k) = i_{c\beta 2}(k) + \frac{C_2}{T_s}\left(u^*_{L\beta}(k) - u_{L\beta}(k)\right) \end{cases}. \tag{17}$$

The output current generation mechanism of the parallel side is shown in Fig. 4.

C. Cost Function

In order to realize independent control of the series and parallel sides, the TSC corresponds to the cost function only for the output current of one side of converters. The value function g_1 is constructed for the output current of the series side

$$g_1 = \left|i^*_{\alpha 1}(k) - i_{\alpha 1}(k+1)\right| + \left|i^*_{\beta 1}(k) - i_{\beta 1}(k+1)\right|. \tag{18}$$

The value function g_2 is constructed for the output current of the parallel side

$$g_2 = \left|i^*_{\alpha 2}(k) - i_{\alpha 2}(k+1)\right| + \left|i^*_{\beta 2}(k) - i_{\beta 2}(k+1)\right|. \tag{19}$$

Fig. 5 shows a block diagram of series side control based on indirect control and synchronized rotating coordinate system. The traditional control method consists of detection, control and modulation section. In the detection section, harmonic components to be compensated are identified. However, the effectiveness of power quality compensation is significantly impacted by harmonic detection and the accuracy of phase-locked-loop. The control section involves system coupling within the synchronous rotating coordinate system and four PI controllers, posing challenges for parameter adjustment. Additionally, the modulation section necessitates further processing and calculation of the modulation signal. As a result, the control structure of the NSC-UPQC system under the traditional method is complex, leading to delayed response and difficulty in setting controller parameters.

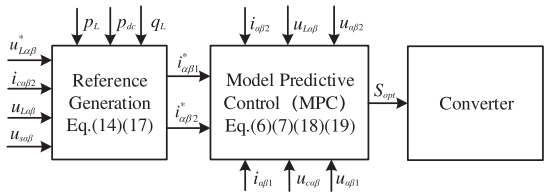

Fig. 6. Block diagram of predictive direct control.

TABLE II
VOLTAGE VECTOR OF INV2 SWITCHING STATE COMPARISON

	V_{l0}	V_{l1}	V_{l2}	V_{l3}	V_{l4}	V_{l5}	V_{l6}	V_{l7}
	000	001	010	011	100	101	110	111
S_{AL}	1	1	1	1	0	0	0	0
S_{BL}	1	1	0	0	1	1	0	0
S_{CL}	1	0	1	0	1	0	1	0

Fig. 6 shows the block diagram of the proposed predictive direct control of NSC-UPQC, which contains only two parts: the given current generation and the model predictive control. The predictive direct control algorithm eliminates the need for PLL, harmonic detection, system coupling, and PI parameter rectification, considerably simplifying the control process.

IV. Time-Sharing Cooperative Control

The performance of the UPQC mainly depends on the accurate and fast tracking of the reference signal. The output of both the series and parallel side of the NSC-UPQC contains eight voltage vectors on one side only at any moment of the TSC mode. This mode results in the overall low output performance of the NSC and poor tracking of reference currents on the series and parallel sides of the NSC-UPQC. Therefore, in this section, building upon TSC, a TSCC approach is proposed for predictive direct control of NSC-UPQC. This aims to optimize the tracking effect of the given current by leveraging the redundancy of NSC's switching device states and introducing the concept of cooperative control.

A. Principles of Vector Selection

It can be seen from (1) and Fig. 2(b) that the eight voltage output vectors $V_{l0}\sim V_{l7}$ of INV2 are only related to S_{AL}, S_{BL}, and S_{CL},which are inversely related to their counterparts.The voltage vectors of INV2 are given in Table II in comparison with S_{AL}, S_{BL}, and S_{CL}.

TABLE III
VOLTAGE VECTOR OF INV1 SWITCHING STATE COMPARISON

	V_{u0}	V_{u1}	V_{u2}	V_{u3}	V_{u4}	V_{u5}	V_{u6}	V_{u7}
	000	001	010	011	100	101	110	111
S_{AU}	0	0	0	0	1	1	1	1
S_{BU}	0	0	1	1	0	0	1	1
S_{CU}	0	1	0	1	0	1	0	1

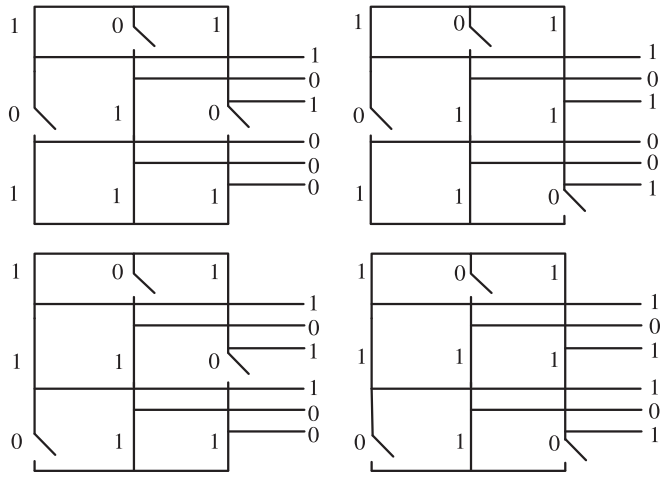

Fig. 7. Schematic diagram of vector selection principle.

It can also be observed from (2) and Fig. 2(a) that the eight voltage output vectors $V_{u0}\sim V_{u7}$ of INV1 are only related to S_{AU}, S_{BU}, and S_{CU}, which are inversely related to their counterparts. The voltage vectors of INV1 are given in Table III in comparison with S_{AU}, S_{BU}, and S_{CU}.

The NSC three phase upper switching device state vector is noted as $S_{up} = [S_{AU}S_{BU}S_{CU}]$, the middle switching device state vector is noted as $S_{\text{middle}} = [S_{AM}S_{BM}S_{CM}]$, and the lower switching device state vector is noted as $S_{\text{low}} = [S_{AL}S_{BL}S_{CL}]$.

INV1 and INV2 under TSC operation can be equated to two independent two-level inverters, where the control performance of either inverter is only related to the eight effective voltage vectors, and the other inverter outputs zero voltage vectors. However, different from the two-level inverters, the switching device states on the upper and lower sides of INV1 and INV2 do not necessarily adhere to the principle of either 1 or 0 when determining the voltage output vector at a certain moment.

As shown in Fig. 7, when INV1 outputs $V_{u5}(101)$, it needs to satisfy $S_{up} = [101]$, and S_{middle} does not necessarily take the inverse [010]. Under the premise of satisfying the NSC topology constraints S_{middle} can take the four states [010], [011], [110], and [111], and the corresponding voltage vectors of INV2 are V_{l0}, V_{l1}, V_{l4}, and V_{l5}, respectively. Therefore, when INV1 determines the optimal action vector, the states of S_{middle} and S_{low} are not unique, and INV2 can output non-zero voltage vectors to put into operation. This selection principle aligns with the constraint condition of the NSC switching device. Even after determining the vector output of one end, the switching device retains the redundant state necessary for normal operation.

TABLE IV
VOLTAGE VECTOR OF INV2 CORRESPONDS TO THE SWITCHING STATES AND VOLTAGE VECTOR OF INV1

INV2	$S_{up}S_{\text{middle}}$	INV1
V_{l0}	000111,011100,001110,101010, 010101,110001,100011,111000	V_{u0} V_{u1} V_{u2} V_{u3} V_{u4} V_{u5} V_{u6} V_{u7}
V_{l1}	101011,111001,001111,011101	V_{u1} V_{u3} V_{u5} V_{u7}
V_{l2}	111010,110011,011110,010111	V_{u2} V_{u3} V_{u6} V_{u7}
V_{l3}	011111,111011	V_{u3} V_{u7}
V_{l4}	100111,111100,101110 ,110101	V_{u4} V_{u5} V_{u6} V_{u7}
V_{l5}	101111,111101	V_{u5} V_{u7}
V_{l6}	110111,111110	V_{u6} V_{u7}
V_{l7}	111111	V_{u7}

TABLE V
VOLTAGE VECTOR OF INV1 CORRESPONDS TO THE SWITCHING STATES AND VOLTAGE VECTOR OF INV2

INV1	$S_{\text{middle}}S_{\text{low}}$	INV2
V_{u0}	111111	V_{l0}
V_{u1}	110111,111110	V_{l0} V_{l1}
V_{u2}	101111,111101	V_{l0} V_{l2}
V_{u3}	100111,111100,101110 ,110101	V_{l0} V_{l1} V_{l2} V_{l3}
V_{u4}	011111,111011	V_{l0} V_{l4}
V_{u5}	111010,110011,011110,010111	V_{l0} V_{l1} V_{l4} V_{l5}
V_{u6}	101011,111001,001111,011101	V_{l0} V_{l2} V_{l4} V_{l6}
V_{u7}	000111,011100,001110,101010, 010101,110001,100011,111000	V_{l0} V_{l1} V_{l2} V_{l3} V_{l4} V_{l5} V_{l6} V_{l7}

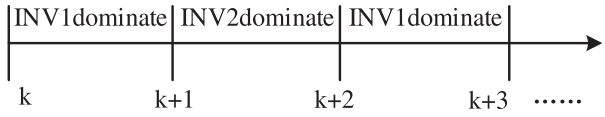

Fig. 8. Mechanism of TSCC.

Table IV gives the corresponding switching device states and the selectable range of voltage vectors on the parallel side after determining the voltage vectors on the series side.

Table V gives the corresponding switching device states and series side voltage vector selectable ranges after determining the parallel side voltage vector.

B. Mechanism of TSCC

The mechanism of TSCC is demonstrated in Fig. 8, where two control cycles form a complete cycle. In the previous control cycle, the series side predominates, while in the subsequent control cycle, the parallel side takes precedence. The first part of the operation is carried out at moment k to predict the optimal switching signal to act at moment $k+1$, while the second part of the operation is performed at moment $k+1$ to predict the optimal switching signal to act at moment $k+2$, etc.

1) *First Control Cycle*: Cost function $g1$ is calculated according to the series side prediction model (6), the reference current (14), and the cost function (18). The series side cost function g_1 is optimized by 8 times of voltage vector

TABLE VI
UPQC PARAMETERS

Parameters	Value
Grid RMS voltage(u_s)	220 V
Grid frequency	50 Hz
Series side capacitance(C_1)	0.2 μF
Series side inductance(L_1)	50 mH
Parallel side capacitance(C_2)	300 μF
Parallel side inductance (L_2)	4 mH
DC voltage (V_{dc})	1200 V
DC link capacitors(C_{dc})	5500 μF
Sampling period (T_s)	80 μs

rolling to obtain the optimal action vector of the series side. As long as the optimal action vector is selected, the parallel side cost function g_2 is optimized by rolling to obtain the optimal action vector of the parallel side according to the corresponding switching device states and the optional range of voltage vectors of the parallel side in Table IV. The optimal action vectors required on the parallel side are obtained, and all the switching device signals are then obtained.

2) *Second Control Cycle*: Cost function g_2 is calculated following the parallel side prediction model (7), the reference current (17), and the cost function (19). The parallel side cost function g_2 is optimized by eight times of voltage vector rolling to obtain the optimal action vector of the parallel side. As long as the optimal action vector is selected, the series side cost function g_1 is optimized by rolling to obtain the optimal action vector of the series side according to the corresponding switching device states and the optional range of voltage vectors of the series side in Table IV. The optimal action vectors required on the series side are obtained, and all the switching device signals are then obtained.

V. SIMULATION AND HARDWARE-IN-LOOP TEST ANALYSIS

To validate the proposed NSC-UPQC predictive direct control method based on TSCC, MATLAB/Simulink and an hardware-in-loop (HIL) test platform with digital signal processor (DSP), field programmable gate array (FPGA), and Typhoon HIL402 are also employed.

A. Simulation Results

According to IEC 61000-4-30 standard. Voltage swell/sag is a sudden increase/decrease in voltage of 10% or more above the normal or recommended operating voltage within a period of 1/2 cycle to 1 min. The system is designed to create a 15% temporary voltage swell at 0.1 s, a 15% temporary voltage sag at 0.2 s, and the introduction of voltage harmonic at 0.3 s. Table VI gives the system parameters. This article employs the finite control set model predictive control method, which is characterized by a variable switching frequency. Based on simulation statistics, the average switching frequency is 2.72 kHz when the system control period is 80 μs.

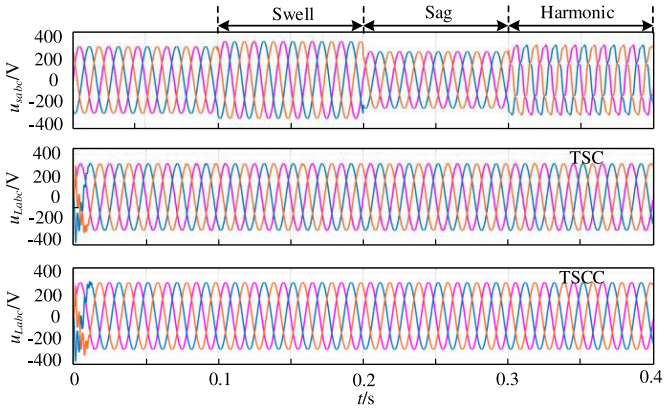

Fig. 9. Voltage compensation effect.

TABLE VII
THD OF VOLTAGE COMPENSATION WITH DIFFERENT CONTROL METHODS

Method	Conditon	THD%
TSC	Voltage swell	1.20
	Voltage sag	1.24
	Voltage harmonic	1.28
TSCC	Voltage swell	0.92
	Voltage sag	0.89
	Voltage harmonic	0.94

The voltage compensation effects of the NSC-UPQC predictive direct control strategy are compared using TSC and TSCC, as shown in Fig. 9. The figure illustrates that the proposed strategy effectively compensates for transient voltage increases, decreases, and harmonics in the grid voltage amplitude.

Table VII gives a comparison of harmonic distortion rates for voltage compensation.

Fig. 10 depicts the simulation waveforms of load voltages under 0.1 s grid voltage swell, 0.2 s grid voltage sag, and 0.3 s grid voltage harmonic moments, comparing traditional control methods with predictive direct control based on TSCC. It is evident that traditional control methods exhibit voltage fluctuations during changes in grid voltage, whereas predictive direct control shows smoother and smaller fluctuations. Due to its avoidance of harmonic component detection and PLL, predictive direct control mitigates control delays caused by these factors, resulting in faster response compared to traditional control methods.

Fig. 11 presents a comparative chart of the current compensation effects of the predictive direct control strategy using two control methods. It can be clearly seen that the TSC method struggles to maintain sinusoidal characteristics in the grid side current, indicating significant waveform distortion issues. In comparison, the TSCC method proves to be more effective in maintaining sinusoidal grid side currents and demonstrates stronger compensatory effects.

Table VIII gives the harmonic distortion rates for current compensation under these two different control methods.

In order to research the control effect of the system parameter mismatch, this article provide an example using the mismatch

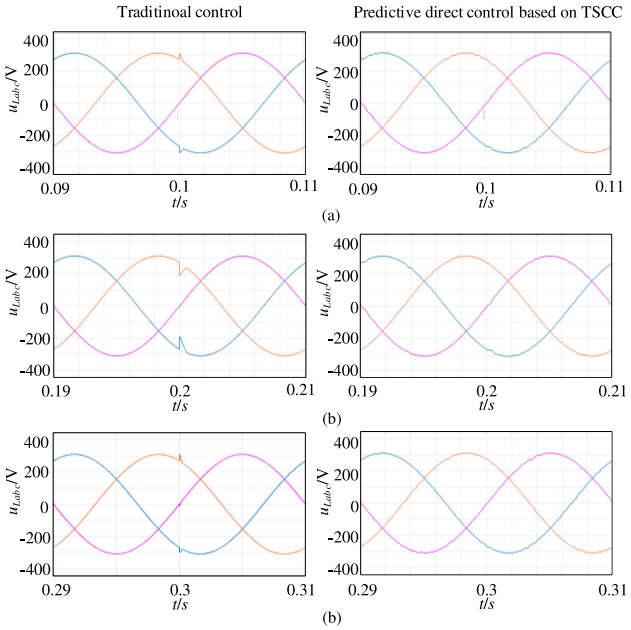

Fig. 10. Load voltage waveforms at different moments for two methods. (a) Voltage swell. (b) Grid voltage sag. (b) Grid voltage harmonic.

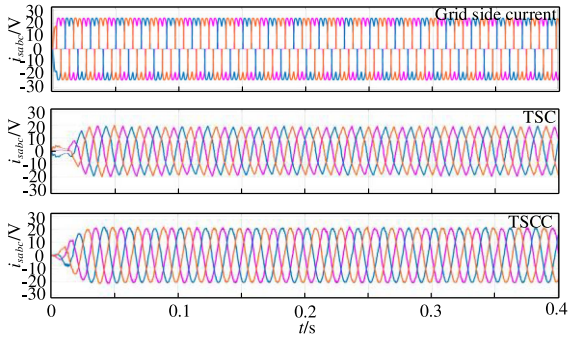

Fig. 11. Current compensation effect.

TABLE VIII
THD OF CURRENT COMPENSATION WITH DIFFERENT METHODS

Method	Conditon	THD%
TSC	Voltage swell	4.87
	Voltage sag	5.23
	Voltage harmonic	4.96
TSCC	Voltage swell	2.80
	Voltage sag	2.63
	Voltage harmonic	2.89

of inductance parameter L_2 in the prediction model under the premise of ensuring approximate consistency of switching frequencies. Specifically, when L_2 is set to 0.5, 1.0, and 1.5 times the actual value. We present the THD of the load voltage under three operating conditions: grid voltage swell; voltage sag; and voltage harmonic. These results are compared with the effects of traditional indirect compensation control using a PI regulator, as shown in Fig. 12. As depicted, the traditional linear control method does not face parameter mismatch issues since it does not rely on a system model. Although the control effect of the method proposed in this article depends on the system model parameters, the control effect is still better than the traditional control method, even when the parameter mismatch reaches 50%.

To validate the tracking accuracy of the proposed TSCC method for the reference current, Fig. 13 illustrates waveform images of the series side output current and the reference current. This example focuses on the α-axis of the series side, considering the current under two control methods. The TSCC method demonstrates significantly superior tracking accuracy for the current phase and amplitude compared to the TSC method.

Setting a higher dc-bus voltage enables the converter to have a wider output range and therefore the UPQC obtains a more favorable compensation effect. Since the dc side voltage utilization of the NSC is less compared to the conventional back-to-back two level converter, a larger value of c side voltage is required. Fig. 14 illustrates the dc-bus voltage waveform of the predictive direct control strategy based on the TSCC. Under sudden changes in operating conditions, the dc bus experiences minor fluctuations, but regains its stability quickly.

To assess the dynamic performance of the system and its nonlinear current compensation capabilities under the proposed TSCC method, a nonlinear load is introduce. Fig. 15 illustrates a high distortion rate in the current waveform before NSC activation in the main circuit. However, once NSC is engaged at 0.2 s, the current waveform becomes nearly sinusoidal, aligning quickly with the grid-side voltage in phase.

B. HIL Test Results

To validate the effectiveness of the proposed strategy, an HIL test platform is set up. This platform validates the NSC-UPQC predictive direct control method based on TSCC presented in this article, as depicted in Fig. 16.

The primary circuit model is implemented in the Typhoon HIL402 platform, with output pulses generated by the HDSP-DF28335P controller. Harmonic distortion levels of the current are assessed using the HIOKI power quality analyzer PQ3198. The test parameters remain consistent with those used in the simulation section. The parameters for the IGBT were set as follows: dead time of 5 μs, snubber type R of 1×10^5 Ω, and C of 1×10^{-6} μF. Nominal power of the transformer was 2000 VA.

1) Performance of Predictive Direct Control Based on TSCC Under Normal Voltage Condition: When the three-phase input grid voltage is normal and a nonlinear load is connected, the HIL test results are depicted in Fig. 17.

Fig. 17(a) and (b) shows that the strategy not only maintains the load voltage at the set amplitude of 311 V, but also controls the phase deviation between the load voltage and the grid voltage. As illustrated in Fig. 17(c) and (d), the grid current is effectively sinusoidalized, and the grid side power factor is controlled to be 1. Fig. 17(e) and (f) indicates that the THD of the load voltage and the grid current are 1.88% and 3.00%, respectively.

2) Performance of Predictive Direct Control Based on TSCC Under Voltage Swell Condition: Fig. 18 illustrates the HIL test

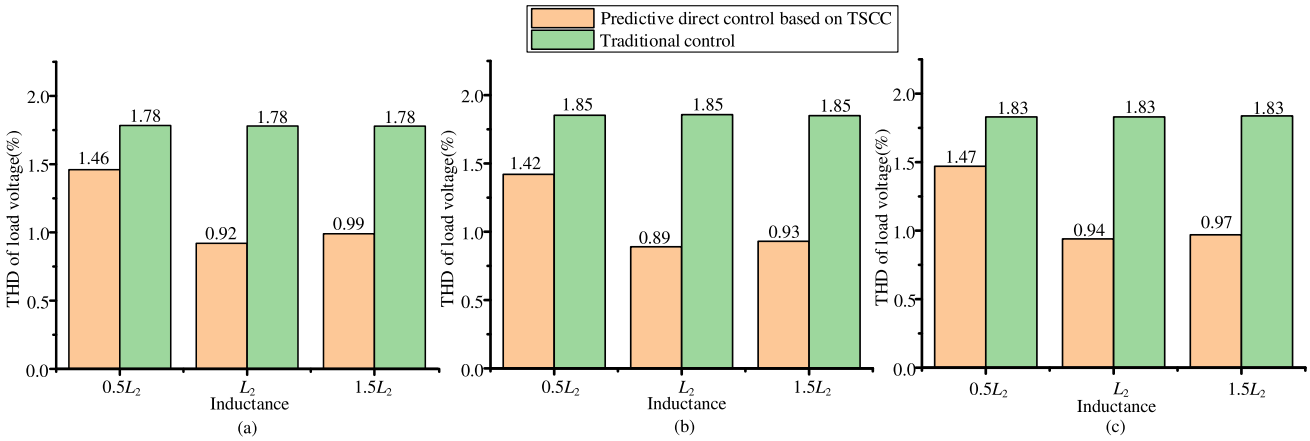

Fig. 12. Parameter mismatch performance of the two control methods under different operating conditions. (a) Voltage swell condition. (b) Voltage sag condition. (c) Voltage harmonic condition.

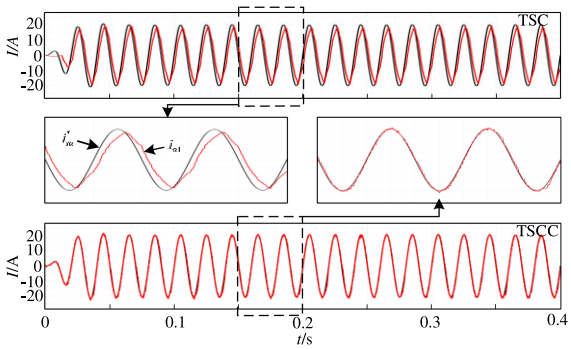

Fig. 13. Tracking effect for reference current.

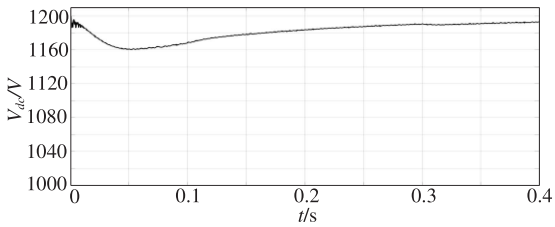

Fig. 14. DC-bus voltage waveform.

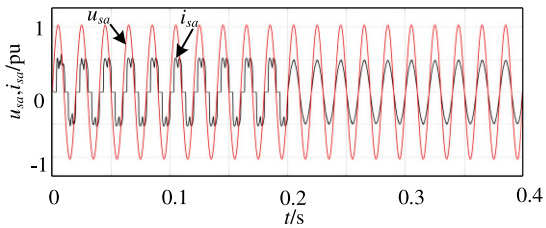

Fig. 15. Phase grid side voltage and current.

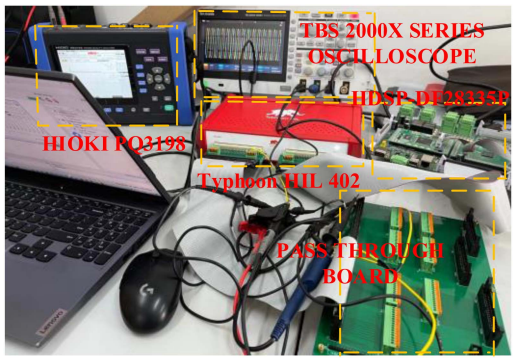

Fig. 16. HIL test platform.

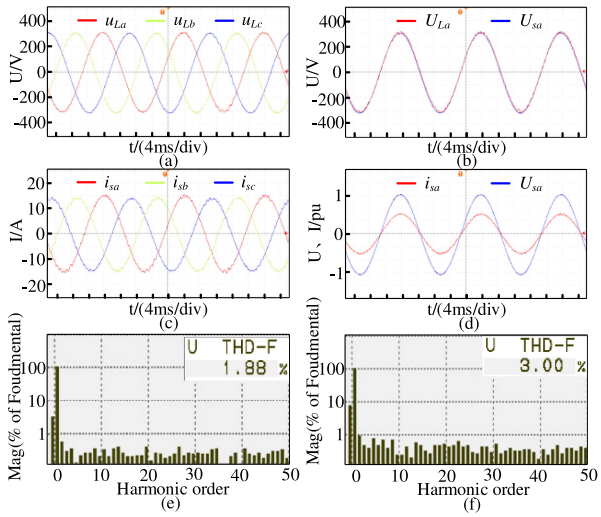

Fig. 17. Normal voltage condition. (a) Load voltage. (b) Phase load voltage and grid voltage. (c) Grid current. (d) Phase grid current and grid voltage. (e) Load voltage THD. (f) Grid current THD.

results of a transient 15% increase in the three-phase input grid voltage due to the connection of a nonlinear load.

Fig. 18(a) and (b) reveals that the UPQC predictive direct control strategy based on TSCC under the voltage swell condition not only maintains the load voltage as a sinusoidal waveform with constant amplitude and retains the stability of the user-side voltage, but also has the same phase as the grid voltage. Fig. 18(c) and (d) illustrates that the grid current is effectively sinusoidalized, and that the power factor of the control grid side

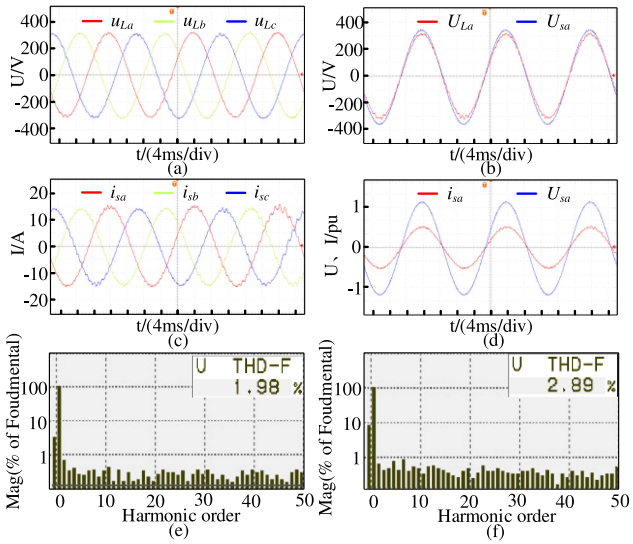

Fig. 18. Voltage swell condition. (a) Load voltage. (b) Phase load voltage and grid voltage. (c) Grid current. (d) Phase grid current and grid voltage. (e) Load voltage THD. (f) Grid current THD.

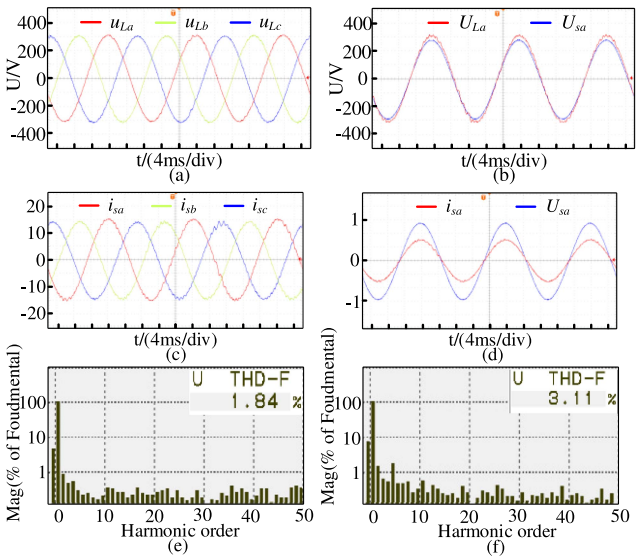

Fig. 19. Voltage sag condition. (a) Load voltage. (b) Phase load voltage and grid voltage. (c) Grid current. (d) Phase grid current and grid voltage. (e) Load voltage THD. (f) Grid current THD.

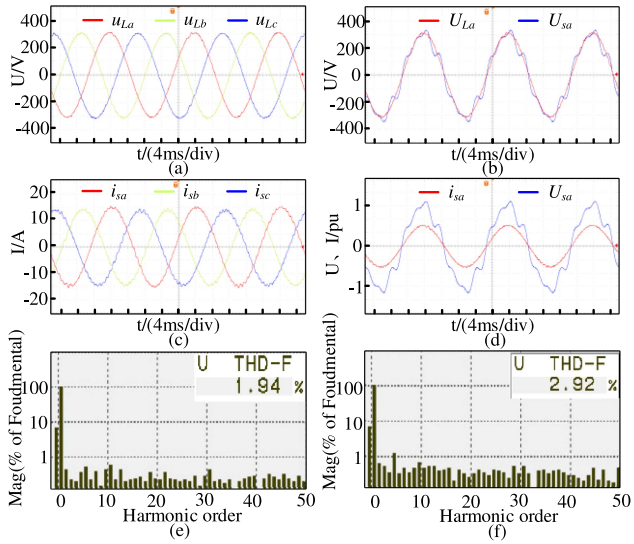

Fig. 20. Voltage harmonic condition. (a) Load voltage. (b) Phase load voltage and grid voltage. (c) Grid current. (d) Phase grid current and grid voltage. (e) Load voltage THD. (f) Grid current THD.

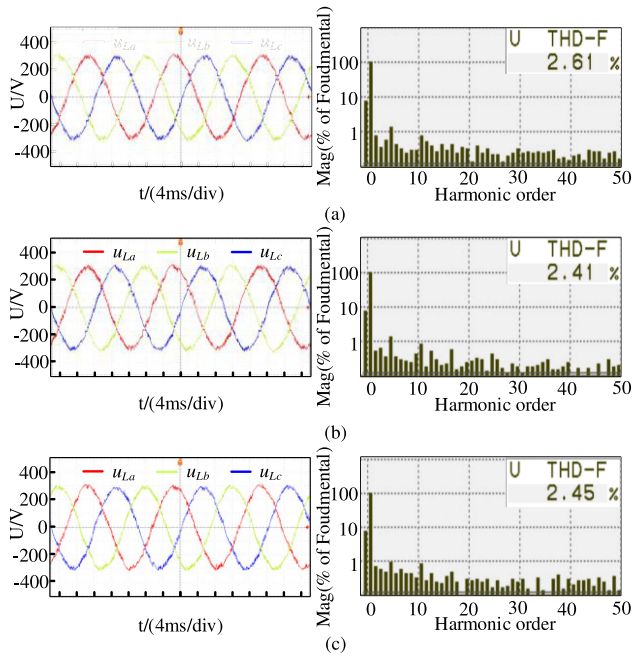

Fig. 21. Waveforms of load voltage and its THD under different working conditions of traditional control. (a) Voltage swell. (b) Voltage sag. (c) Voltage harmonic.

is 1. Fig. 18(e) and (f) demonstrates the THDs of the load voltage and the grid current of 1.98% and 2.89% after the compensation, respectively, effectively maintaining the system stability.

3) Performance of Predictive Direct Control Based on TSCC Under Voltage Sag Condition: Fig. 19 presents the HIL test results of a transient 15% decrease in the three-phase input grid voltage due to the connection of a nonlinear load.

As shown in the figure, the proposed strategy can realize the sinusoidalization of load voltage and grid current, and the change of grid voltage does not affect the power factor change at the grid side. The THD of load voltage and grid current after compensation is depicted in Fig. 19(e) and (f). Under the UPQC predictive direct control strategy based on TSCC, the THD of load voltage is 1.84%, and the THD of grid current is 2.63%, effectively improving the power quality problems present in the system.

4) Performance of Predictive Direct Control Based on TSCC Under Voltage Harmonic Condition: Fig. 20 displays the HIL test results of the three-phase input grid voltage when it exhibits 14% harmonics due to the connection of a nonlinear load.

It can be observed from Fig. 20 that although there are quality problems in the power side voltage due to harmonics, the grid current and load voltage maintain sinusoidal waves with constant

TABLE IX
THD COMPARISON WITH DIFFERENT CONTROL METHODS

Working conditions	Traditional control		Predictive direct control based on TSC		Predictive direct control based on TSCC	
	Load voltage	Grid current	Load voltage	Grid current	Load voltage	Grid current
Voltage swell	2.61	3.11	2.16	4.97	1.98	2.89
Voltage sag	2.41	3.24	2.43	5.42	1.84	3.11
Voltage harmonic	2.45	3.28	2.28	5.18	1.94	2.92

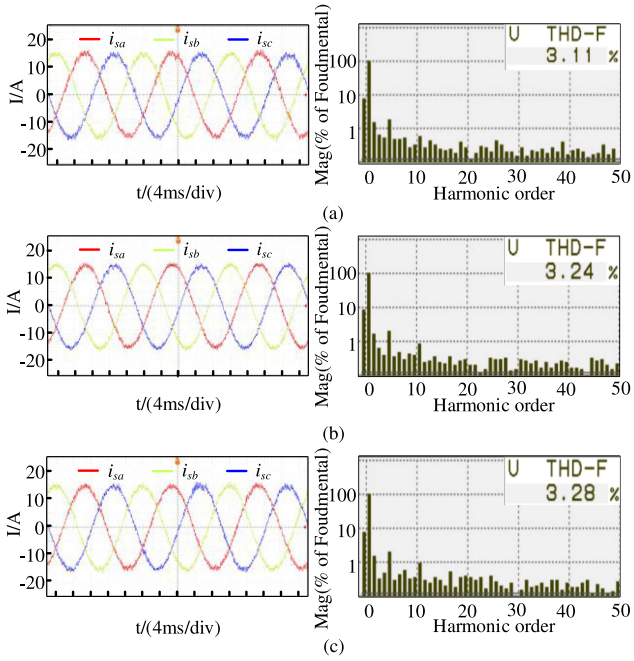

Fig. 22. Waveforms of grid current and its THD under different working conditions of traditional control. (a) Voltage swell. (b) Voltage sag. (c) Voltage harmonic.

amplitude under the UPQC predictive direct control strategy based on TSCC. At the same time, the power factor of the system is always 1. Fig. 20(e) and (f) shows that the THDs of the load voltage and the grid current are 1.94% and 2.92%, respectively, with the system power quality problem effectively improved.

Figs. 21 and 22 illustrate the load voltage and grid current waveforms under voltage swell, voltage sag, and harmonic conditions for the traditional PI control. These steady-state data were obtained from the HIL test platform. Comparing with the effect of predictive direct control based on TSCC proposed in this article. It reveals that under all tested conditions, both the load voltage and grid current THD are higher with traditional control methods than with the predictive direct control methods based on TSC and TSCC proposed in this article. Table IX gives the THD of load voltage and grid current for traditional PI control, TSC-based predictive direct control, and TSCC-based predictive direct control across various operating conditions. It is evident that the predictive direct control method based on TSCC outperforms the other methods in both voltage and current control effectiveness, validating the efficacy of the proposed control approach.

VI. CONCLUSION

To conclude, a predictive direct control strategy was hereby proposed based on TSCC for NSC-UPQC, addressing challenges encountered in indirect control, including harmonic detection, response delays from PLL, system coupling due to coordinate transformation, and the complexity of PI parameter tuning. First, the predictive direct control model under $\alpha\beta$ coordinate system was constructed by combining direct control with FCS-MPC. Second, based on the principle of power balance of the system, the reference current generation mechanism on the series side under $\alpha\beta$ coordinate system was constructed. Meanwhile, the reference current generation mechanism on the parallel side under $\alpha\beta$ coordinate system was constructed by combining the principle of dead-beat with the principle of constant amplitude of the load voltage. The system achieved complete decoupling, eliminating the need for harmonic detection, PLL, and PI parameter adjustments, thereby significantly simplifying the controller structure. Finally, building upon TSC and leveraging the redundancy of NSC's switching device states, the TSCC method was proposed by establishing control vector selection principles and control mechanisms. TSCC improved the tracking accuracy of the reference current, and achieved better current and voltage compensation effect. Through simulation and HIL test analysis, it was hereby confirmed that the proposed algorithm had better compensation accuracy in voltage transient swell, transient sag and harmonic power quality problems, and could realize the stable and efficient operation of NSC-UPQC.

REFERENCES

[1] N. Lin, S. Cao, and V. Dinavahi, "Comprehensive modeling of large photovoltaic systems for heterogeneous parallel transient simulation of integrated AC/DC grid," *IEEE Trans. Energy Convers.*, vol. 35, no. 2, pp. 917–927, Jun. 2020.

[2] H. Li, C. Lv, and Y. Zhang, "Research on new characteristics of power quality in distribution network," in *Proc. IEEE Int. Conf. Power, Intell. Comput. Syst.*, 2019, pp. 6–10.

[3] P. K. Ray, S. R. Das, and A. Mohanty, "Fuzzy-controller-designed-PV-based custom power device for power quality enhancement," *IEEE Trans. Energy Convers.*, vol. 34, no. 1, pp. 405–414, Mar. 2019.

[4] T. Tanaka, K. Ma, H. Wang, and F. Blaabjerg, "Asymmetrical reactive power capability of modular multilevel cascade converter based STATCOMs for offshore wind farm," *IEEE Trans. Power Electron.*, vol. 34, no. 6, pp. 5147–5164, Jun. 2019.

[5] H. Zhang, C. da Sun, Z.-X. Li, J. Liu, H.-Y. Cao, and X. Zhang, "Voltage vector error fault diagnosis for open-circuit faults of three-phase four-wire active power filters," *IEEE Trans. Power Electron.*, vol. 32, no. 3, pp. 2215–2226, Mar. 2017.

[6] J. Yu, W. Shi, J. Li, L. Deng, and M. Pei, "A discrete-time non-adaptive SOGI-based frequency-locked Loop," *IEEE Trans. Power Syst.*, vol. 35, no. 6, pp. 4912–4915, Nov. 2020.

[7] D. Ramirez, S. Martinez, C. A. Platero, F. Blazquez, and R. M. de Castro, "Low-voltage ride-through capability for wind generators based on dynamic voltage restorers," *IEEE Trans. Energy Convers.*, vol. 26, no. 1, pp. 195–203, Mar. 2011.
[8] V. Khadkikar, "Enhancing electric power quality using UPQC: A comprehensive overview," *IEEE Trans. Power Electron.*, vol. 27, no. 5, pp. 2284–2297, May 2012.
[9] L. Zhang, P. C. Loh, and F. Gao, "An Integrated nine-switch power conditioner for power quality enhancement and voltage SAG mitigation," *IEEE Trans. Power Electron.*, vol. 27, no. 3, pp. 1177–1190, Mar. 2012.
[10] S Mabusubani and S Kornepati, "Comparison of PI and ANN control techniques for nine switchs UPQC to improve power quality," *Int. J. Sci. Eng. Technol. Res.*, vol. 3, no. 33, pp. 6565–6581, Aug. 2014.
[11] J. Guo, L. Sun, and K. Zhao, "Modulation strategy of UPQC based on nine-switch converter," *Elect. Power Automat. Equip.*, vol. 36, no. 10, pp. 78–84, Jan. 2016.
[12] Y. Xue, Y. F. Ren, and Z. S. Hu, "Control strategy of direct drive-doubly fed distributed wind power system based on nine-switch converter," *Automat. Elect. Power Syst.*, vol. 46, no. 7, pp. 152–159, Dec. 2022.
[13] M. Anand and P. Kumar, "Fuzzy controller based topologies of NS-UPQC and B4-UPQC," in *Proc IEEE Int. Conf. Advent Trends Multidisciplinary Res. Innov.*, 2020, pp. 1–7.
[14] S. Vijayasamundiswary and J. Baskaran, "A novel approach to nine switch unified power quality conditioner for power quality improvement," in *Proc. Int. Conf. Innov. Res. Elect. Sci.*, 2017, pp. 1–5.
[15] J. Wang, K. Sun, H. Wu, J. Zhu, Y. Xing, and Y. Li, "Hybrid connected unified power quality conditioner integrating distributed generation with reduced power capacity and enhanced conversion efficiency," *IEEE Trans. Ind. Electron.*, vol. 68, no. 12, pp. 12340–12352, Dec. 2021.
[16] R. A. Modesto, S. A. O. da Silva, A. A. de Oliveira, and V. D. Bacon, "A versatile unified power quality conditioner applied to three-phase four-wire distribution systems using a dual control strategy," *IEEE Trans. Power Electron.*, vol. 31, no. 8, pp. 5503–5514, Aug. 2016.
[17] S. Kouro, P. Cortes, R. Vargas, U. Ammann, and J. Rodriguez, "Model predictive control—A simple and powerful method to control power converters," *IEEE Trans. Ind. Electron.*, vol. 56, no. 6, pp. 1826–1838, Jun. 2009.
[18] Y. Gao, T. Yang, T. Dragičević, S. Bozhko, P. Wheeler, and C. Zheng, "Optimal filter design for power converters regulated by FCS-MPC in the MEA," *IEEE Trans. Power Electron.*, vol. 36, no. 3, pp. 3258–3268, Mar. 2021.
[19] C. R. Baier, R. O. Ramirez, E. I. Marciel, J. C. Hernández, P. E. Melín, and E. E. Espinosa, "FCS-MPC without steady-state error applied to a grid-connected cascaded H-bridge multilevel inverter," *IEEE Trans. Power Electron.*, vol. 36, no. 10, pp. 11785–11799, Oct. 2021.
[20] V. Jayan and A. Ghias, "Finite control set model predictive control of a nine switch dual output converter as a power quality conditioner," in *Proc. IEEE Int. Conf. Ind. Technol.*, 2019, pp. 1241–1246.
[21] O. Gulbudak and E. Santi, "Model predictive control of dual-output nine-switch inverter with output filter," in *Proc. IEEE Energy Convers. Congr. Expo.*, 2015, pp. 1582–1589.
[22] O. Gulbudak and M. Gokdag, "Asymmetrical multi-step direct model predictive control of nine-switch inverter for dual-output mode operation," *IEEE Access*, vol. 7, pp. 164720–164733, 2019.
[23] C. Liu, B. Wu, N. R. Zargari, D. Xu, and J. Wang, "A novel three-phase three-leg AC/AC converter using nine IGBTs," *IEEE Trans. Power Electron.*, vol. 24, no. 5, pp. 1151–1160, May 2009.
[24] T. Furuhashi, S. Okuma, and Y. Uchikawa, "A study on the theory of instantaneous reactive power," *IEEE Trans. Ind. Electron.*, vol. 37, no. 1, pp. 86–90, Feb. 1990.

Guifeng Wang (Member, IEEE) was born in Linyi, Shandong, China, in 1982. He received the B.S. degree in electrical engineering and automation, the M.S. degree in electrical engineering from the School of Information and Electrical Engineering, China University of Mining and Technology, Xuzhou, China, in 2004 and 2007, respectively, and the Ph.D. degree in power electronics and electrical drive from Shanghai Jiao Tong University, Shanghai, China, in 2016. He is currently a Senior Engineer with the College of Electrical Engineering and Automation, Jiangsu Normal University, Xuzhou, China.

His current research interests include power electronic converters for electrical drives and power quality.

Yunhui Jiang was born in Nantong, China, in 1998. He received the B.S. degree in automation from Jiangsu Ocean University, Lianyungang, China, in 2021. He is currently working toward the M.S. degree in electronic information with the Jiangsu Normal University, Xuzhou, China.

His current research interests include power electronics and electric machines drives.

Zhan Liu (Member, IEEE) was born in Anhui, China, in 1989. He received the B.S. degree in electrical engineering and automation, the M.S. degree in power electronics and power drives, and the Ph.D. degree in electrical engineering from China University of Mining and Technology, Xuzhou, Jiangsu, China, in 2011, 2013, and 2016.

Since 2017, he has been an Associate Professor with the School of Electrical Engineering and Automation, Jiangsu Normal University, China, where he is responsible for a National Natural Science Foundation of China. He has authored or coauthored more than four papers on IEEE T-PE and T-PE. His research interests include power electronics, modern control theory, model predictive control and multilevel Converter.

Yiming Ma was born in Suqian, China, in 1998. He received the B.S. degree in automation from Xian Polytechnic University, Xian, China, in 2020. He is currently working toward the M.S. degree in electronic information with the Jiangsu Normal University, Xuzhou, China.

His current research interests include power electronics converters and power systems.

Jianfei Wang was born in Suichuan, Jiangxi, China in 2000. He received the B.S. degree in electrical engineering and automation from Nanchang Hangkong University, Nanchang, China, in 2022. He is currently working toward the M.S. degree in electronic information with Jiangsu Normal University, Xuzhou, China.

His current research interests include power electronic converter design and model predictive current control techniques.